Strain-induced ferroelectricity and spin-lattice coupling in $SrMnO_3$ thin films

J. W. Guo,[1] P. S. Wang,[2] Y. Yuan,[3] Q. He,[4,*] J. L. Lu,[2] T. Z. Chen,[1] S. Z. Yang,[1] Y. J. Wang,[1] R. Erni,[5] M. D. Rossell,[5] V. Gopalan,[3] H. J. Xiang,[2,6,†] Y. Tokura,[7] and P. Yu[1,7,8,‡]

[1]*State Key Laboratory of Low Dimensional Quantum Physics and Department of Physics, Tsinghua University, Beijing 100084, China*

[2]*Key Laboratory of Computational Physical Sciences (Ministry of Education), State Key Laboratory of Surface Physics, and Department of Physics, Fudan University, Shanghai 200433, China*

[3]*Department of Materials Science and Engineering and Materials Research Institute, Pennsylvania State University, University Park, Pennsylvania 16802, USA*

[4]*Department of Physics, Durham University, Durham DH1 3LE, United Kingdom*

[5]*Electron Microscopy Center, Empa, Swiss Federal Laboratories for Materials Science and Technology, CH-8600 Dubendorf, Switzerland*

[6]*Collaborative Innovation Center of Advanced Microstructures, Nanjing 210093, People's Republic of China*

[7]*RIKEN Center for Emergent Matter Science (CEMS), Saitama 351-0198, Japan*

[8]*Collaborative Innovation Center of Quantum Matter, Beijing 100084, China*

(Received 6 January 2018; published 20 June 2018)

Designing novel multiferroic materials with simultaneous ferroelectric and magnetic orders has been one of the focal points over the last decade due to the promising applications and rich physics involved. In this study, using epitaxial strain (up to 3.8%) as tuning knob, we successfully introduce multiferroicity with prominent high-temperature ferroelectricity into the paraelectric $SrMnO_3$. More interestingly, the experimental temperature-dependent ferroelectric and magnetic studies suggest that the emergent antiferromagnetic order below 100 K greatly enhances the ferroelectric polarization due to the spin-order-induced ionic displacements. We envision that the strain-mediated spin-phonon coupling can be utilized as a pathway to discover functionalities in a wide range of antiferromagnetic insulators with delicate epitaxial manipulations.

DOI: 10.1103/PhysRevB.97.235135

Multiferroic materials with simultaneously ferroelectric and magnetic orders have attracted tremendous research interests because of their fundamental scientific importance as well as potential applications [1–5]. Accordingly, searching for novel multiferroic materials has been one of the central questions for related studies; among variable approaches (e.g., exploiting Bi 6*s* lone pairs [6], spin ordering [7], superlattice [8], octahedral rotation [9], etc.), strain engineering stands out as one of the most effective pathways [10]. Recent theoretical calculations have predicted that the external epitaxial strain can couple with the lowest-frequency polar phonon and drive the antiferromagnetic-paraelectric $EuTiO_3$ into a ferromagnetic-ferroelectric multiferroic [11], which was later experimentally realized [12]. However, the low ferromagnetic transition temperature (∼4 K) of $EuTiO_3$ due to its relatively low intrinsic Néel temperature limits its practical applications. Thus research focuses turn into materials with higher magnetic transition temperature, and it was theoretically proposed that epitaxial strain could stabilize the polar state in antiferromagnetic-paraelectric $SrMnO_3$ (SMO) [13] and other manganite systems [14,15] and lead to superior multiferroicity with higher transition temperature. This prediction was soon confirmed in bulk SMO by partially substituting strontium with barium, which induced negative chemical pressure and led to a polar ferroelectric state [16]. Although a rich phase diagram has been proposed recently for a strained manganite sample from theoretical aspects [17–19], the experimental studies in SMO thin films and other related manganite systems so far have been limited to small tensile strain cases (∼1.6%) [20–25], and the study for larger tensile strain remains as a great challenge due to the difficulty to maintain the strain state of the film and obtain correct oxygen stoichiometry in synthesizing these samples [26–28].

In this work, high-quality SMO thin films were successfully synthesized with tunable biaxial tensile strain (up to 3.8%) with selected substrates. With the highly strained sample, we observed the direct evidence of ferroelectricity with the ferroelectric transition temperature well above room temperature. The large remnant polarization (∼55 $\mu C/cm^2$) observed strongly highlights the prominent ferroelectric performance comparable to conventional ferroelectric materials. More interestingly, our studies reveal that in the highly strained samples, the emergence of the antiferromagnetic spin state (theoretically determined as *C*-type antiferromagnetic order) enhances the ferroelectric order as a consequence of the strong correlation between spin-lattice coupling and strain-induced polar instability.

I. RESULTS

A. Fabrication and characterization of highly strained $SrMnO_3$ thin films

Our experiments were performed on 10-nm-thick commensurate $(001)_{pc}$-oriented SMO films grown on

*qing.he@durham.ac.uk
†hxiang@fudan.edu.cn
‡yupu@tsinghua.edu.cn

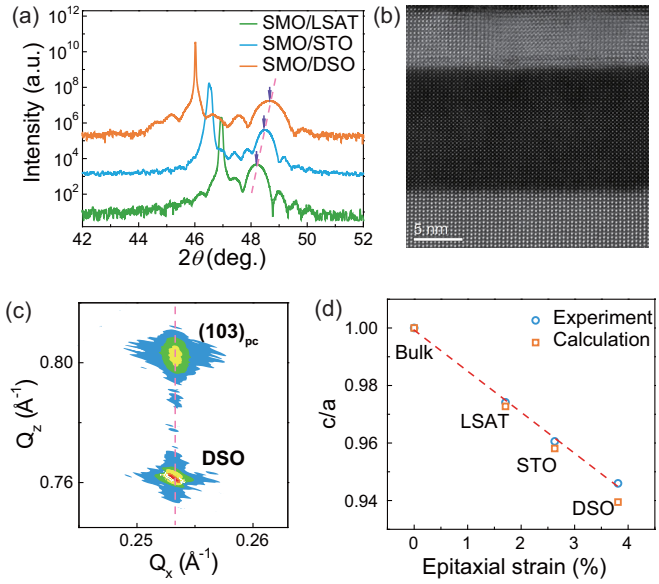

FIG. 1. Structural characterizations of high-quality epitaxial thin films. (a) X-ray diffraction θ-2θ scans for SMO thin films grown on LSAT (green), STO (blue), and DSO (orange) substrates in the vicinity of out-of-plane $(002)_{pc}$ SMO reflection, where the subscript refers to the pseudocubic (pc) index. (b) Cross-sectional high-angle annular dark field image of the strained SMO thin film (dark region) grown on DSO substrate (bright regions). A thin DSO layer (top regions) was employed as capping layer. The image shows coherent growth between the SMO and DSO substrate with a sharp interface and low density of defects within the film. (c) Reciprocal-space mapping of the SMO film grown on the DSO substrate, demonstrating a coherent and epitaxial growth. (d) c/a ratio (tetragonality) of SMO films as a function of epitaxial strain. The orange square shows the DFT calculated results for comparison.

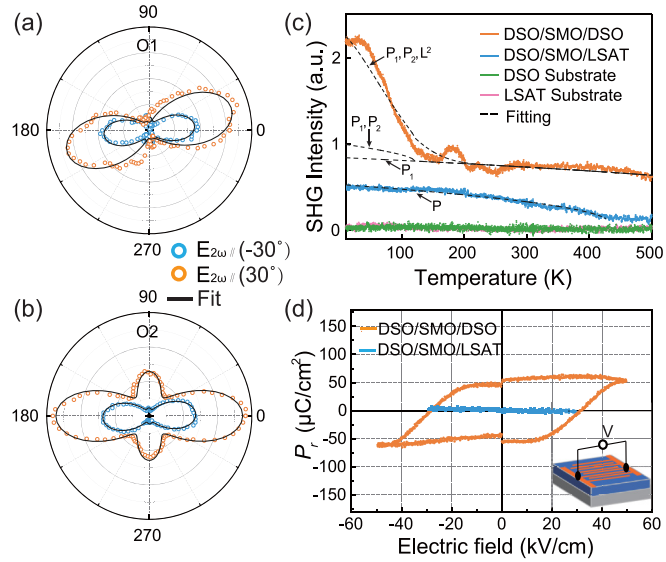

FIG. 2. Evidence of ferroelectricity in highly strained $SrMnO_3$ thin films. (a), (b) Experimental SHG polar plots (at 4 K) of the highly strained SMO films grown on DSO substrates with sample orientations of O1 and O2, respectively. Domains with monoclinic symmetry were used in the fitting, which indicates the existence of both in-plane and out-of-plane polarization components. (c) Temperature-dependent SHG response for SMO thin films grown on DSO (orange line) and LSAT (light-blue line) substrates with reference data taken on bare DSO (green line) and LSAT (pink line) substrates. The dashed lines show the fitting results using polar and magnetic model. (d) In-plane remnant ferroelectric hysteresis loops for SMO thin films grown on DSO (orange line) and LSAT (blue line) substrates measured at 10 K with the frequency of 1 kHz. The results were obtained with the PUND method, which probes directly the switchable and remnant ferroelectric polarization.

$(001)_{pc}(LaAlO_3)_{0.3}(Sr_2AlTaO_6)_{0.7}$ (LSAT), $(001)_{pc}$ $SrTiO_3$ (STO), and $(110)_o$ $DyScO_3$ (DSO) substrates with reflection high-energy electron diffraction (RHEED)-assisted pulsed-laser deposition (PLD) method (Supplemental Material Fig. 1 [29]). We note that the strained SMO thin film can very easily degrade in air by forming cracks in the film (as shown in Supplemental Material Fig. 2 [29]), which will in turn relax the epitaxial strain and make it a large challenge to probe directly the intrinsic properties of this interesting material at a high strain state. To prevent the strained samples from degradation, we developed an 8-nm-thick $DyScO_3$ as a capping layer, which can make the films stable over a large range of strain states. Figure 1(a) shows typical x-ray diffraction (XRD) θ-2θ scans for SMO films grown on different substrates. The well-defined SMO diffraction peaks and clear Kiessig fringes indicate a high crystalline quality of the samples as well as their interfaces, which are also confirmed by the clear RHEED pattern and intensity oscillation during growth (Supplemental Material Fig. 1 [29]). Moreover, the cross-sectional scanning transmission electron microscopy (STEM) images [a typical image is shown in Fig. 1(b)] also reveal the film to be highly commensurate and the interface is atomically abrupt. The sandwiched SMO layer was further investigated with rocking curve scans around the SMO (002) Bragg peak, and the full width at half maximum ($\sim$0.06°) is close to that of the substrates ($\sim$0.03°), implying a great crystallinity as well. To obtain the epitaxial relationship between SMO layers and substrates, reciprocal-space mappings (Fig. 1(c) and Supplemental Material Fig. 3 [29]) were performed. The close match of the in-plane lattice constants of the SMO layers to the corresponding substrates indicates that the SMO samples are fully strained. With the knowledge on both in-plane and out-of-plane lattice constants, the tetragonality (c/a ratio) can then be obtained as shown in Fig. 1(d), which is $\sim$0.945 for the highly strained sample (SMO/DSO sample), providing a promising condition to introduce ferroelectricity.

B. Ferroelectricity in the highly strained samples

The optical second-harmonic generation (SHG) measurements (see Methods and Supplemental Material Fig. 4 [29]) were carried out to detect the breaking of inversion symmetry, which is a necessity to host ferroelectricity [30]. The fact that the STO substrate gives an enormous SHG background signal makes it impossible to study the SMO layer alone, thus only the results for SMO/DSO and SMO/LSAT samples are presented in Fig. 2 (as well as the following studies), from which well-defined SHG signals were obtained in the heterostructures, while both DSO and LSAT substrates give negligible contributions. The SHG polarimetry measurements

of SMO/DSO were performed at both 4 K [Figs. 2(a) and 2(b)] and room temperature (Supplemental Material Fig. 5 [29]) by recording the SHG signal while rotating the polarization of the fundamental beam. Theoretical modeling of the polarimetry results reveals a monoclinic symmetry of the system, suggesting that the electrical polarization not only has a large component along the pseudocubic ⟨110⟩ in-plane direction, but also a small [001] out-of-plane contribution.

We note that the breaking of inversion symmetry and arising of spontaneous polarization (P_l) can give SHG intensity in the form [31] of $I^{2\omega} \propto \chi^2_{ijkl} P_l^2$, where χ_{ijkl} is susceptibility tensor allowed in the centrosymmetric parent phase. The temperature-dependent polarization across the first-order transition can be written as $P_l = P_0[(1/2) + (1/2)\sqrt{(T_1 - T)/(T_1 - T)_c}]$, where T_c is Curie temperature, T_1 is the upper bound of phase coexistence temperature. With these equations, the temperature-dependent SHG signal [Fig. 2(c)] can be further analyzed. Accordingly, SMO/LSAT exhibits a polar transition at $T_c = 420$ K with a fitting value of 433 K for T_1, which is very close to the ferroelectric transition obtained in the $Sr_{0.5}Ba_{0.5}MnO_3$ bulk [16] and SMO/LSAT thin film [24]. The nice agreement between experimental data and theory modeling suggests that the SHG signal from SMO/LSAT can be well explained by the emergence of spontaneous polarization below 420 K, while no other transition was observed. For the higher strained system, SMO/DSO, the SHG signal is clearly enhanced with the polar phase persisting until 560 K, above which the film is irreversibly changed with the evidence shown in Supplemental Material Fig. 7 [29]. Moreover, different from the case of the SMO/LSAT, the SHG signal of the SMO/DSO sample exhibits an interesting upturn around 120 K. Theoretical modeling by considering only one polar transition, P_1, with Curie temperature above 560 K, shows a clear disagreement below 120 K. Interestingly, by introducing a second-order polar transition P_2 at 120 K, the deviation between theory and experiment becomes smaller. However, according to density-functional theory (DFT) calculations presented later, the magnitude of the second polarization (spin-induced ferroelectric component) at 0 K is estimated to be $P_2 \approx 10\%\ P_1$. Thus, this large enhancement of SHG below 120 K cannot be explained only by the polar transitions. Since SMO is expected to establish antiferromagnetic ordering at low temperature, it is possible to dramatically enhance the SHG signal. By adopting the method in previous study [31], we consider the contribution of the antiferromagnetic order to the SHG as $I^{2\omega}_{AFM} \propto I^{2\omega}_0[1 - (T/T_0)^{3/2}]^4$, where T_0 is the magnetic and polar orders coupling formation temperature. Taking this contribution into our model for SMO/DSO, we obtained a good agreement between theory and experiment with T_0 of 255 K. Note that although the magnetic ordering is likely to emerge simultaneously with P_2 at 120 K, this magnetic and polar coupling is proved to be able to persist into the paramagnetic state, thus well above the magnetic transition temperature [31,32].

In order to further investigate the ferroelectricity of the strained SMO films, the ferroelectric hysteresis loops were measured by the positive-up negative-down (PUND) method [33], with the interdigital electrode configuration as shown in the inset of Fig. 2(d), from which only the remnant polarization is obtained. The measurement on the SMO/DSO sample [Fig. 2(d), in orange] reveals a well-defined hysteresis loop at 10 K with the remnant polarization (P_r) of $\sim 55\ \mu C/cm^2$ along the in-plane direction. We note that this remnant polarization is comparable to conventional ferroelectric materials (e.g., $BaTiO_3$) suggesting the prominent ferroelectric nature of the highly strained sample. In contrast, the SMO/LSAT sample exhibits no loop behavior with the electric field up to 30 kV/cm, above which the electric breakdown occurs with dramatically enhanced leakage current. To shed more light on the strain-induced ferroelectric polarization, a strain-relaxed DSO/SMO/DSO sample (with the c/a ratio changed from 0.945 to 0.97) was also measured, in which however no remnant ferroelectric polarization was observed. This detailed comparison is consistent with the previous local spin density approximation plus on-site Coulomb repulsion (LSDA+U) result [13], which indicates that larger tensile strain (+3.6%) is desired to achieve the ferroelectricity in SMO.

C. Strain tuning of antiferromagnetic ordering and spin-lattice coupling in SMO films

The previous first-principles calculations [13] predicted that large tensile strain could drive the SMO film into a ferromagnetic state. However, macroscopic magnetic measurements on our present sample with strain up to 3.8% (Supplemental Material Fig. 8 [29]) shows no detectable remnant magnetization down to ~10 K, indicating that the system retains its antiferromangetic state [34]. In order to investigate the magnetic nature of the highly strained SMO films, x-ray absorption spectroscopy (XAS) and x-ray linear dichroism (XLD) were employed to probe the antiferromagnetic state [35]. Figure 3(a) [Fig. 3(b)] presents typical XAS of the Mn L edges with the polarization (E-field direction) of the incident light in close parallel (olive green) and perpendicular (in orange) to the (001) direction of the crystal with the SMO/LSAT (SMO/DSO) films. The XLD spectra, as shown in Figs. 3(c) and 3(d), are then extracted from the difference between the XAS spectra taken with different polarizations. We note that the high-energy side of the Mn L_3 edge (between 643 and 648 eV) strongly overlaps with the Dy M edges because of the second-harmonic contamination of the beamline EPU; thus, only the spectra taken below 643 eV and over the L_2 edge were used for further analysis. For both SMO/LSAT and SMO/DSO samples, the turn-up of the Mn L_3 edge at the same energy position (~639 eV), and the almost identical characteristic energy for the L_2 edge strongly suggest that the samples maintain good oxygen stoichiometry despite the great different strain states.

We note that in some multiferroics, such as $BiFeO_3$, both antiferromagnetic and ferroelectric orders can contribute to the XLD signal [36]. Thus, temperature-dependent XLD studies were employed here to separate their contributions. To avoid the second-harmonic contamination of Dy from the capping layer, only the Mn L_2 edges were used for the studies, which show distinct XLD features at the characteristic energies of 651.4 and 652.7 eV [marked as A and B peaks in Figs. 3(c) and 3(d)]. The XLD amplitudes were then extracted using the asymmetry of the peak intensity between A and B peaks ($I_{XLD} = I_{A-B}/I_{A+B}$) and plotted in Fig. 3(e) as a function of temperature. The SMO/LSAT sample shows an obvious

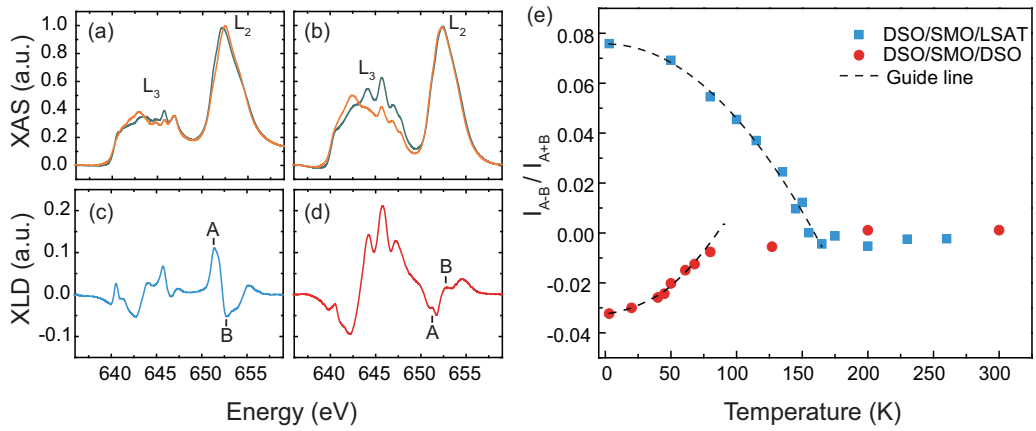

FIG. 3. The strain-engineered magnetic orders in $SrMnO_3$ thin films. Representative Mn L-edge XAS results for SMO samples grown on (a) LSAT and (b) DSO substrates. The measurements were carried out at 3 K with the total fluorescence yield mode. Olive-green and orange lines represent the results with horizontal and vertical polarized x-ray, respectively. (c) and (d) represent the corresponding x-ray linear dichroism results. (e) Temperature evolution of the I_{XLD}, ratio of I_{A-B} to I_{A+B}. A and B represent the XLD intensities at 651.4 and 652.7 eV, respectively.

transition at ∼160 K, while the SHG measurement reveals ferroelectric phase transition only at 420 K in this sample. Hence, in the current SMO system, the XLD signal is mainly attributed to the antiferromagnetic order, and the XLD transition temperature should be assigned as the antiferromagnetic Néel temperature ($T_N = 160$ K), which shows excellent agreement with the previous experimental result [34]. In comparison, the XLD spectra on the highly strained SMO/DSO sample show reversed features at the energies of 651.4 and 652.7 eV, pointing to a distinct antiferromagnetic easy axis from that of the SMO/LSAT. The corresponding temperature-dependent result shows a transition at ∼80 K, which can be attributed to the newly established antiferromagnetic transition according to the previous theoretical work [13], as well as our theoretical analysis as discussed later. It is worth noting that the observed polar state well above 80 K by SHG does not contribute to significant XLD signal, which again suggests that the contribution of ferroelectric orders to the XLD is rather small. The coincidence of the transition temperature where the antiferromagnetic and enhanced ferroelectricity [Fig. 2(c)] emerge very likely indicates a strong coupling between the antiferromagnetic state and the great enhancement of the ferroelectric polarization at SMO/DSO sample.

D. First-principles DFT calculations

In order to provide further theoretical insights into the magnetic and ferroelectric natures of the strained SMO films, first-principles DFT calculations (see Methods) were carried out. Firstly, the distortions of the cubic perovskite parent phase (space group $Pm\bar{3}m$) of SMO were studied under various epitaxial strain states. For this purpose, global searches were performed for the lowest-energy structures at each epitaxial strain based on the genetic algorithm (GA) specially designed to optimize structural distortions [37,38]. The calculated lattice constants and especially the strain-dependent tetragonality show remarkable consistency with the experimental results [Fig. 1(d)]. Then, the magnetic and ferroelectric ground states of the SMO films were further investigated at various strain states with the energy profile and ferroelectric polarization shown in Figs. 4(a) and 4(b). The theoretical calculation predicts that SMO remains a G-type antiferromagnetic order for the small strain state, and then starts to favor C-type antiferromagnetic configuration at higher strains [Fig. 4(a)]. Moreover, the ferroelectric polarization is also predicted to be further enhanced with the larger strain state. For the bulk state, the SMO film is paraelectric because the lowest-energy crystal structure has a $C2/c$ nonpolar symmetry; for the SMO films with tensile strain larger than 1% the lowest-energy crystal structure turns into $Ima2$ for all magnetic states [Fig. 4(b)], which is consistent with the prediction by Lee and Rabe [13]. At the tensile strain of 3.8%, the calculated ferroelectric polarization is along the pseudocubic $[\bar{1}10]$ direction with the polarization magnitude of 47.11 $\mu C/cm^2$, in nice agreement with the experimental results. Because of the cubic symmetry of the bulk SMO and the biaxial tensile strain employed, there are four symmetrically equivalent ⟨110⟩ directions. Accordingly, the electric polarization could be along one of these four ⟨110⟩ axes, consistent with our SHG polarimetry. We note that SHG also suggests the existence of a small out-of-plane polarization along [001] direction, which is likely due to the presence of two inequivalent interfaces in the DSO capped heterostructure.

To shed light on the magnetic nature of the highly strained sample, we constructed three-dimensional magnetic configurations by analyzing the strain-induced bond angle modulation as well as the consequent changes of nearest-neighbor superexchange interactions and the next-nearest neighbor supersuperexchange interactions, as shown in Supplemental Material Fig. 9 [29]. The results suggest that the magnetic ground state emerges into C-type antiferromagnetism, with the antiferromagnetic transition temperature T_N estimated by the mean-field theory around 104 K for the SMO sample with 3.8% tensile strain [Supplemental Material Notes 1 [29] and as shown in Fig. 4(c)], which is qualitatively consistent with the characteristic temperatures observed in SHG and XLD studies. The results can be explained in term of the Goodenough-Kanamori rule [39,40], where the antiferromagnetically coupled exchange interaction between d^3-d^3 ions is strongly

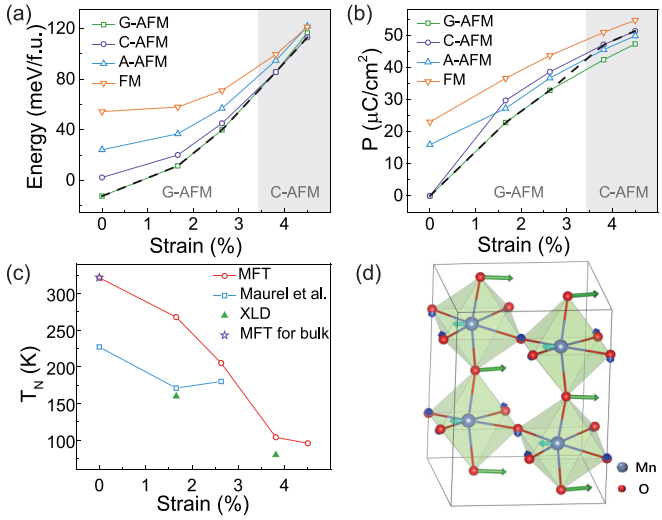

FIG. 4. First-principles calculations of ferroelectric and magnetic orderings in strained $SrMnO_3$ thin films. (a) Total energy of SMO as a function of epitaxial strain with different magnetic states. The cubic perovskite (i.e., space group $Pm\bar{3}m$) SMO with the *G*-type antiferromagnetic spin order is taken as the energy reference. Black dashed line shows the magnetic ground states for different strains. (b) Ferroelectric polarizations of the lowest-energy SMO structures with the *G*-type antiferromagnetic (green square), *C*-type antiferromagnetic (purple circle), *A*-type antiferromagnetic (blue triangle), and ferromagnetic (orange triangle) spin orders at different strain states. The polarization is along the pseudocubic $[\bar{1}10]$ direction. The black dashed line shows the ferroelectric polarizations of the magnetic ground state. (c) Estimated magnetic transition temperatures (Néel temperature) of SMO at various strain states by the mean-field theory. The blue square shows the previous experimental data [30] to compare with our mean-field theory (MFT) results. The purple star shows Néel temperature of bulk unstrained SMO by the MFT. The green triangle represents the results from our XLD measurements. (d) Calculated crystalline structure of the 3.8% tensile strained SMO with *Ima*2 symmetry. The dark-green vectors represent the ion displacements of the *C*-type antiferromagnetic state relative to that of the *G*-type antiferromagnetic state, which are along the pseudocubic $[\bar{1}10]$ direction.

suppressed and eventually changes into ferromagnetic interaction along the decreasing of the out-of-plane Mn–O–Mn bond angle with tensile strain (Supplemental Material Fig. 10 [29]). Note that we find that not only the Mn–O–Mn bond angle, but also the Mn–O bond length determines the nature of the Mn^{4+}-Mn^{4+} exchange coupling. To be more specific, a larger Mn–O bond length tends to favor a ferromagnetic Mn^{4+}-Mn^{4+} exchange coupling. This explains why the out-of-plane Mn-Mn exchange coupling becomes ferromagnetic when the Mn–O–Mn bond angle is still relatively large (see Supplemental Material Notes 2 [29] for details).

To understand the coupling between the antiferromagnetic state and ferroelectric polarization, we investigated the spin-order-induced polarization. The ferroelectric polarization of the *Ima*2 SMO film at 3.8% strain with *C*-type antiferromagnetism is larger than that with *G*-type antiferromagnetism by $\sim 4.69\,\mu C/cm^2$ (as shown in Supplemental Material Fig. 11 [29]), and the enhanced polarization is along the same direction ($[\bar{1}10]$ direction) as the total polarization of the *C*- and *G*-type antiferromagnetic phases (Supplemental Material Fig. 12 [29]). We then carried out further analysis using the recently developed unified polarization model of spin-order-induced polarization [41] to see which mechanism is mainly responsible for the enhancement of the electric polarization. Our DFT calculations reveal that the pure electronic, ion-displacement, and lattice deformation contributions (i.e., P_e, P_{ion}, and P_{def}) to the spin-order-induced polarization enhancement can be estimated as 0.45, 4.30, and $-0.06\,\mu C/cm^2$, respectively. Therefore, we can conclude that the ion-displacement contribution forms the dominating mechanism responsible for the spin-order-induced polarization. We further investigated the underlying microscopic mechanism by considering the spin-lattice energy, as discussed in detail in Supplemental Material Note 3 and Supplemental Material Figs. 13 and 14 [29]. We find the spin-order-induced polarization by *C*-type antiferromagnetism is larger than that of *G*-type antiferromagnetism by $5.4\,\mu C/cm^2$, which is close to the direct DFT result ($4.3\,\mu C/cm^2$). Our analysis demonstrates clearly that the oxygen ions move along the $[1\bar{1}0]$ direction to minimize the ferromagnetic out-of-plane Mn-Mn exchange interaction energy in the *C*-type antiferromagnetic phase, which subsequently enhances the polarization along the $[\bar{1}10]$ direction. Therefore, it can be concluded that the polarization enhancement below T_N is mainly due to the spin-order-induced ion displacements (i.e., the exchange-striction mechanism [42–44]) in the *C*-type antiferromagnetic state with large tensile strain.

II. SUMMARY

In summary, we have experimentally demonstrated the strain-induced multiferroicity in SMO thin films showing simultaneous high-temperature ferroelectricity and antiferromagnetism. The direct remnant ferroelectric hysteresis measurement reveals a polarization up to $55\,\mu C/cm^2$ at 10 K, on a par with the value of type I multiferroic materials (e.g., $BiFeO_3$). Furthermore, the enhancement of ferroelectric polarization below the magnetic transition temperature for the highly strained samples suggests a spin-lattice coupling mechanism, in which the spin order leads to further ionic displacements and consequently enhancement of the ferroelectric polarization. Thus, the present study identifies strained SMO thin films as a high-temperature multiferroic model system with intriguing magnetoelectric coupling. Finally, we expect that the strain-mediated spin-phonon coupling can be well extended into a wide range of antiferromagnetic insulators with delicate epitaxial manipulation.

III. METHODS

A. Thin-film growth

High-quality epitaxial thin films were grown by the RHEED-assisted PLD method. The SMO and DSO thin films were grown at 850 °C in a dynamic oxygen pressure of 0.15 mbar on various substrates enabling variable strain states. The laser energy (KrF, $\lambda = 248$ nm) was fixed at $1.4\,J/cm^2$ with repetition rate of 5 Hz. After the growth, the samples were cooled down to room temperature with 1 atm oxygen at cooling rate of 10 °C/min.

B. Structural characterization

The crystalline structure of thin films was analyzed by XRD and reciprocal space mapping measurements by four-circle x-ray diffractometer (Rigaku Smartlab). The sample for transmission electron microscopy measurements was prepared in cross section by means of an FEI Helios Nanolab 450S focused ion-beam instrument. The high-resolution *Z*-contrast image was acquired in STEM mode with a high-angle annular dark field (HAADF) detector using a double-spherical aberration-corrected JEOL JEM-ARM200F microscope operated at 200 kV. The annular semidetection range of the annular dark-field detector was calibrated at 90–170 mrad.

C. Ferroelectric polarization measurements

Ferroelectric polarization hysteresis loops were measured using a Precision Multiferroic test system (Radiant Technologies). The in-plane ferroelectric polarization is probed through an interdigital electrode device geometry as shown in Fig. 2(d). The length of interdigital electrodes is 575 μm, and the distance between the two electrodes is 5 μm, which is much larger than film thickness of 10 nm. 50-nm Au with 10-nm Ti as buffer layer was employed as the electrode for the electric contact during the measurements. To avoid the possible leakage contribution, the PUND method was employed to probe directly only the remnant polarization during the switching.

D. SHG measurements

The SHG response was measured with a far-field transmission geometry using an 800-nm fundamental laser beam generated by a Spectra-Physics SOLSTICE ACE Ti: sapphire femtosecond laser system (<100 fs, 1 kHz). The experimental configuration is shown in Supplemental Material Fig. 4 [29], where a linear polarized fundamental light is incident to the sample at a tilted angle of θ defined by the sample normal and optical axis. The second-harmonic signal ($E_{2\omega}$) generated through the nonlinear optical process within the sample is then decomposed into *p*-polarized ($E_{2\omega//}$) and *s*-polarized ($E_{2\omega\perp}$) components by a polarizing beam-splitter. For each sample, SHG polar plots were obtained by measuring the SHG response through rotating the incident polarization φ at fixed θ. Theoretical fitting of the SHG polarimetry data was performed by the method described in previous work [45], in which the nonlinear optical d_{ij} tensor for monoclinic symmetry was written as

$$d_{ij}=\begin{pmatrix} 0 & 0 & 0 & 0 & d15 & d16 \\ d21 & d22 & d23 & d24 & 0 & 0 \\ d31 & d32 & d33 & d34 & 0 & 0 \end{pmatrix}.$$

Two sample orientations (O1 and O2) were employed during the measurements, which were defined as $O1:\{Z_1=[\bar{1}10], Z_2=[001], Z_3=[110]\}$ and $O2:\{Z_1=[001], Z_2=[1\bar{1}0], Z_3=[110]\}$ under DSO orthorhombic notation in our study. During simulations, we considered four possible domain configurations with mirror symmetry along one of the SMO pseudocubic (110), $(1\bar{1}0)$, $(\bar{1}10)$, or $(\bar{1}\bar{1}0)$ planes, while for SMO/LSAT sample, two sample orientations were defined similarly as $O1:\{Z_1=[100], Z_2=[010], Z_3=[001]\}$ and $O2:\{Z_1=[010], Z_2=[\bar{1}00], Z_3=[001]\}$ under cubic notation of the LSAT substrate. Four possible domain configurations were then considered with mirror symmetry along LSAT cubic (110), $(\bar{1}10)$, $(\bar{1}\bar{1}0)$, and $(1\bar{1}0)$ planes.

With these assignments, the SHG intensity can be described as

$$O1:\begin{cases} I^{total}_{2\omega||}=w_1 I_{2\omega||}(\beta=45^\circ)+w_2 I_{2\omega||}(\beta=135^\circ)+w_3 I_{2\omega||}(\beta=225^\circ)+(1\text{-}w_1\text{-}w_2\text{-}w_3) I_{2\omega||}(\beta=315^\circ) \\ I^{total}_{2\omega\perp}=w_1 I_{2\omega\perp}(\beta=45^\circ)+w_2 I_{2\omega\perp}(\beta=135^\circ)+w_3 I_{2\omega\perp}(\beta=225^\circ)+(1\text{-}w_1\text{-}w_2\text{-}w_3) I_{2\omega\perp}(\beta=315^\circ) \end{cases},$$

$$O2:\begin{cases} I^{total}_{2\omega||}=w_1 I_{2\omega||}(\beta=135^\circ)+w_2 I_{2\omega||}(\beta=225^\circ)+w_3 I_{2\omega||}(\beta=315^\circ)+(1\text{-}w_1\text{-}w_2\text{-}w_3) I_{2\omega||}(\beta=405^\circ) \\ I^{total}_{2\omega\perp}=w_1 I_{2\omega\perp}(\beta=135^\circ)+w_2 I_{2\omega\perp}(\beta=225^\circ)+w_3 I_{2\omega\perp}(\beta=315^\circ)+(1\text{-}w_1\text{-}w_2\text{-}w_3) I_{2\omega\perp}(\beta=405^\circ) \end{cases},$$

where $w_1, w_2, w_3, 1\text{-}w_1\text{-}w_2\text{-}w_3$ are volume fractions of the four possible domain configurations, $I_{2\omega||}$ and $I_{2\omega\perp}$ are SHG intensities calculated from d_{ij} tensor after considering transmittance and reflectance, and β is the sample rotation angle about its surface normal axis.

E. X-ray absorption and linear dichroism measurements

Soft x-ray absorption experiments were performed at Beamline I06 at the Diamond Light Source. The measurements were done with the incident angles of 30° while tuning the polarizations of the linearly polarized light between horizontal and nearly vertical configurations. Due to existence of the DSO capping layer, bulk sensitive total fluorescence yield mode was selected to probe the Mn *L* edges. The spectra normalization was done with the photon flux measured by the photocurrent of a clean gold mesh. The measurement temperature was set at the range from 3 to 300 K.

F. First-principles calculations

The theoretical calculations were performed with the DFT plus the on-site repulsion (U) method [46] within the generalized gradient approximation [47] on the basis of the projector augmented-wave (PAW) method [48,49] implemented in the Vienna *Ab initio* Simulation Package (VASP) [50,51]. The PAW potentials explicitly include 10 valence electrons for Sr ($4s^2\,4p^6\,5s^2$), 13 for Mn ($3p^6\,3d^5\,4s^2$), and 6 for oxygen ($2s^2\,2p^4$). The plane-wave cutoff energy was set to 500 eV. For the Brillouin-zone sampling, a $4\times4\times3$ k-point mesh was used for the 20-atom unit cell. Following previous DFT+U studies on $SrMnO_3$ [13], the on-site repulsion (U) and exchange

parameter (J) for Mn were chosen as 2.7 and 1 eV, respectively. We adopted the original DFT+U formulation proposed by Liechtenstein *et al.* [46] to treat the 3d electron correlations in Mn. Note that Lee *et al.* adopted the simplified DFT+U formulation [52] proposed by Dudarev *et al.* To search for the lowest-energy crystalline-structure, we adopted a global optimization method based on the GA specially designed for finding the optimal structural distortion [37,38]. We note that our approach is different from the common GAs in the following aspects: (1) To generate an initial structure of the first generation, we first randomly select a subgroup of the space group of the undistorted structure. By symmetrizing a structure with random distortions using the symmetry operation of the subgroup, an initial structure can be obtained with this selected subgroup symmetry. (2) For the mating operation, we propose another crossover operation besides the conventional cut-and-splice method. In our GA simulation, DFT was adopted to relax the structure and compute the total energy. In these DFT calculations, the G-type antiferromagnetic order was assumed. Our test calculations with the C-type antiferromagnetic order gives the same results. The number of atoms in the supercell was fixed to 20. The population size and number of generations were set to 24 and 15, respectively. After the GA global search, we then relaxed the obtained optimal structures with different magnetic order, i.e., G-, A-, and C-type antiferromagnetism, and ferromagnetism at each epitaxial strain state. The in-plane lattice constants were fixed while the out-plane lattice constant and the internal coordinates were fully optimized. For the calculation of ferroelectric polarization, the Berry phase method [53,54] was employed.

ACKNOWLEDGMENTS

This work was financially supported by the National Basic Research Program of China (Grant No. 2015CB921700) and National Natural Science Foundation of China (Grant No. 11274194). Work at Durham University was supported by the Engineering and Physical Sciences Research Council (Grant No. EP/N016718/1). Work at Fudan University was partially supported by Program for Professor of Special Appointment (Eastern Scholar), Qing Nian Ba Jian Program, and Fok Ying Tung Education Foundation. Y.Y. and V.G. were supported by the US Department of Energy, Office of Basic Energy Sciences under Grant No. DE-SC00012375 for the work on optical second-harmonic generation.

J.W.G., P.S.W., and Y.Y. contributed equally to this work.

[1] N. A. Spaldin and M. Fiebig, Science **309**, 391 (2005).
[2] D. I. Khomskii, J. Magn. Magn. Mater. **306**, 1 (2006).
[3] R. Ramesh and N. A. Spaldin, Nat. Mater. **6**, 21 (2007).
[4] S. W. Cheong and M. Mostovoy, Nat. Mater. **6**, 13 (2007).
[5] Y. Tokura, S. Seki, and N. Nagaosa, Rep. Prog. Phys. **77**, 076501 (2014).
[6] R. Seshadri and N. A. Hill, Chem. Mater. **13**, 2892 (2001).
[7] T. Kimura, T. Goto, H. Shintani, K. Ishizaka, T. Arima, and Y. Tokura, Nature (London) **426**, 55 (2003).
[8] J. A. Mundy, C. M. Brooks, M. E. Holtz, J. A. Moyer, H. Das, A. F. Rébola, J. T. Heron, J. D. Clarkson, S. M. Disseler, Z. Liu, A. Farhan, R. Held, R. Hovden, E. Padgett, Q. Mao, H. Paik, R. Misra, L. F. Kourkoutis, E. Arenholz, A. Scholl, J. A. Borchers, W. D. Ratcliff, R. Ramesh, C. J. Fennie, P. Schiffer, D. A. Muller, and D. G. Schlom, Nature (London) **537**, 523 (2016).
[9] N. A. Benedek, A. T. Mulder, and C. J. Fennie, J. Solid State Chem. **195**, 11 (2012).
[10] D. G. Schlom, L. Chen, C. J. Fennie, V. Gopalan, D. A. Muller, X. Pan, R. Ramesh, and R. Uecker, MRS Bull. **39**, 118 (2014).
[11] C. J. Fennie and K. M. Rabe, Phys. Rev. Lett. **97**, 267602 (2006).
[12] J. H. Lee, L. Fang, E. Vlahos, X. Ke, Y. W. Jung, L. F. Kourkoutis, J. W. Kim, P. J. Ryan, T. Heeg, M. Roeckerath, V. Goian, M. Bernhagen, R. Uecker, P. C. Hammel, K. M. Rabe, S. Kamba, J. Schubert, J. W. Freeland, D. A. Muller, C. J. Fennie, P. Schiffer, V. Gopalan, E. J. Halperin, and D. G. Schlom, Nature (London) **466**, 954 (2010).
[13] J. H. Lee and K. M. Rabe, Phys. Rev. Lett. **104**, 207204 (2010).
[14] S. Bhattacharjee, E. Bousquet, and P. Ghosez, Phys. Rev. Lett. **102**, 117602 (2009).
[15] J. M. Rondinelli, A. S. Eidelson, and N. A. Spaldin, Phys. Rev. B **79**, 205119 (2009).
[16] H. Sakai, J. Fujioka, T. Fukuda, D. Okuyama, D. Hashizume, F. Kagawa, H. Nakao, Y. Murakami, T. Arima, A. Q. R. Baron, Y. Taguchi, and Y. Tokura, Phys. Rev. Lett. **107**, 137601 (2011).
[17] H. Chen and A. J. Millis, Phys. Rev. B **94**, 165106 (2016).
[18] A. Marthinsen, C. Faber, U. Aschauer, N. A. Spaldin, and S. M. Selbach, MRS Commun. **6**, 182 (2016).
[19] A. Marthinsen, S. M. Griffin, M. Moreau, T. Grande, T. Tybell, and S. M. Selbach, Phys. Rev. Mater. **2**, 014404 (2018).
[20] C. Becher, L. Maurel, U. Aschauer, M. Lilienblum, C. Magén, D. Meier, E. Langenberg, M. Trassin, J. Blasco, I. P. Krug, P. A. Algarabel, N. A. Spaldin, J. A. Pardo, and M. Fiebig, Nat. Nanotechnol. **10**, 661 (2015).
[21] R. Guzman, L. Maurel, E. Langenberg, A. R. Lupini, P. A. Algarabel, J. A. Pardo, and C. Magén, Nano Lett. **16**, 2221 (2016).
[22] V. Goian, E. Langenberg, N. Marcano, V. Bovtun, L. Maurel, M. Kempa, T. Prokscha, J. Kroupa, P. A. Algarabel, J. A. Pardo, and S. Kamba, Phys. Rev. B **95**, 075126 (2017).
[23] E. Langenberg, L. Maurel, N. Marcano, R. Guzmán, P. Štrichovanec, T. Prokscha, C. Magén, P. A. Algarabel, and J. A. Pardo, Adv. Mater. Interfaces **4**, 1601040 (2017).
[24] S. Kamba, V. Goian, V. Skoromets, J. Hejtmánek, V. Bovtun, M. Kempa, F. Borodavka, P. Vaněk, A. A. Belik, J. H. Lee, O. Pacherová, and K. M. Rabe, Phys. Rev. B **89**, 064308 (2014).
[25] V. Goian, S. Kamba, F. Borodavka, D. Nuzhnyy, M. Savinov, and A. A. Belik, J. Appl. Phys. **117**, 164103 (2015).
[26] J. M. Rondinelli and N. A. Spaldin, Adv. Mater **23**, 3363 (2011).
[27] U. Aschauer, R. Pfenninger, S. M. Selbach, T. Grande, and N. A. Spaldin, Phys. Rev. B **88**, 054111 (2013).
[28] P. Agrawal, J. Guo, P. Yu, C. Hébert, D. Passerone, R. Erni, and M. D. Rossell, Phys. Rev. B **94**, 104101 (2016).
[29] See Supplemental Material at http://link.aps.org/supplemental/10.1103/PhysRevB.97.235135 for more details about structural characterization, measurements, and calculation.
[30] R. C. Miller, Appl. Phys. Lett. **5**, 17 (1964).
[31] M. O. Ramirez, A. Kumar, S. A. Denev, N. J. Podraza, X. S. Xu, R. C. Rai, Y. H. Chu, J. Seidel, L. W. Martin, S.-Y. Yang, E. Saiz,

J. F. Ihlefeld, S. Lee, J. Klug, S. W. Cheong, M. J. Bedzyk, O. Auciello, D. G. Schlom, R. Ramesh, J. Orenstein, J. L. Musfeldt, and V. Gopalan, Phys. Rev. B **79**, 224106 (2009).

[32] P. A. Fleury, Phys Rev. **180**, 591 (1969).

[33] J. F. Scott, C. A. Araujo, H. Brett Meadows, L. D. McMillan, and A. Shawabkeh, J. Appl. Phys. **66**, 1444 (1989).

[34] L. Maurel, N. Marcano, T. Prokscha, E. Langenberg, J. Blasco, R. Guzmán, A. Suter, C. Magén, L. Morellón, M. R. Ibarra, J. A. Pardo, and P. A. Algarabel, Phys. Rev. B **92**, 024419 (2015).

[35] J. Stöhr and H. C. Siegmann, *Magnetism: From Fundamentals to Nanoscale Dynamics* (Springer, Berlin, 2006), p. 5.

[36] M. B. Holcomb, L. W. Martin, A. Scholl, Q. He, P. Yu, C.-H. Yang, S. Y. Yang, P.-A. Glans, M. Valvidares, M. Huijben, J. B. Kortright, J. Guo, Y.-H. Chu, and R. Ramesh, Phys. Rev. B **81**, 134406 (2010).

[37] P. S. Wang, W. Ren, L. Bellaiche, and H. J. Xiang, Phys. Rev. Lett. **114**, 147204 (2015).

[38] X. Z. Lu, X. G. Gong, and H. J. Xiang, Comput. Mater. Sci. **91**, 310 (2014).

[39] J. B. Goodenough, Phys. Rev. **100**, 564 (1995).

[40] J. Kanamori, J. Phys. Chem. Solids **10**, 87 (1959).

[41] H. J. Xiang, P. S. Wang, M.-H. Whangbo, and X. G. Gong, Phys. Rev. B **88**, 054404 (2013).

[42] S. Picozzi, K. Yamauchi, B. Sanyal, I. A. Sergienko, and E. Dagotto, Phys. Rev. Lett. **99**, 227201 (2007).

[43] X. Z. Lu, M.-H. Whangbo, S. Dong, X. G. Gong, and H. J. Xiang, Phys. Rev. Lett. **108**, 187204 (2012).

[44] G. Giovannetti, S. Kumar, C. Ortix, M. Capone, and J. van den Brink, Phys. Rev. Lett. **109**, 107601 (2012).

[45] T. H. Kim, D. Puggioni, Y. Yuan, L. Xie, H. Zhou, N. Campbell, P. J. Ryan, Y. Choi, J.-W. Kim, J. R. Patzner, S. Ryu, J. P. Podkaminer, J. Irwin, Y. Ma, C. J. Fennie, M. S. Rzchowski, X. Q. Pan, V. Gopalan, J. M. Rondinelli, and C. B. Eom, Nature (London) **533**, 68 (2016).

[46] A. I. Liechtenstein, V. I. Anisimov, and J. Zaanen, Phys. Rev. B **52**, R5467(R) (1995).

[47] J. P. Perdew, K. Burke, and M. Ernzerhof, Phys. Rev. Lett. **77**, 3865 (1996).

[48] P. E. Blöchl, Phys. Rev. B **50**, 17953 (1994).

[49] G. Kresse and D. Joubert, Phys. Rev. B **59**, 1758 (1999).

[50] G. Kresse and J. Furthmüller, Comput. Mater. Sci. **6**, 15 (1996).

[51] G. Kresse and J. Furthmüller, Phys. Rev. B **54**, 11169 (1996).

[52] S. L. Dudarev, G. A. Botton, S. Y. Savrasov, C. J. Humphreys, and A. P. Sutton, Phys. Rev. B **57**, 1505 (1998).

[53] R. D. King-Smith and D. Vanderbilt, Phys. Rev. B **47**, 1651 (1993).

[54] R. Resta, Rev. Mod. Phys. **66**, 899 (1994).